NO PLIF study of hypersonic transition over a discrete hemispherical roughness element

Paul M. Danehy[*], Brett Bathel[†], Christopher Ivey[‡], Jennifer A. Inman[§], Stephen B. Jones[**]

NASA Langley Research Center, Hampton VA, 23681-2199

Nitric oxide (NO) planar laser-induced fluorescence (PLIF) has been use to investigate the hypersonic flow over a flat plate with and without a 2-mm (0.08-in) radius hemispherical trip. In the absence of the trip, for all angles of attack and two different Reynolds numbers, the flow was observed to be laminar and mostly steady. Boundary layer thicknesses based on the observed PLIF intensity were measured and compared with a CFD computation, showing agreement. The PLIF boundary layer thickness remained constant while the NO flowrate was varied by a factor of 3, indicating non-perturbative seeding of NO. With the hemispherical trip in place, the flow was observed to be laminar but unsteady at the shallowest angle of attack and lowest Reynolds number and appeared vigorously turbulent at the steepest angle of attack and highest Reynolds number. Laminar corkscrew-shaped vortices oriented in the streamwise direction were frequently observed to transition the flow to more turbulent structures.

I. Introduction

Predicting the onset of transition from laminar to turbulent flow is one of the greatest unsolved challenges in fluid mechanics. Progress has been made in certain speed regimes and for some carefully constrained problems. For example, empirically-based engineering tools are used by NASA's Space Shuttle Program to predict the transition phenomenon during orbiter's entry.[1] This Boundary Layer Transition Prediction Tool, or *BLT Tool*, predicts transition for non-smooth outer mold lines for protuberances and cavities on the surface. Such protuberances and cavities can be caused by damage to the vehicle, especially on ascent. The BLT tool is critically important for safe shuttle operations because transitional and turbulent heating can be up to an order of magnitude higher than laminar heating on hypersonic entry vehicles. Damage to the shuttle can cause early onset of transition and turbulence, potentially overheating the vehicle. Accurately predicting transition allows informed decisions to be made about repairing damage sites on the heat shield. On STS-114, the BLT Tool informed a decision to pull pieces of protruding gap filler in an on-orbit space-walk.[1] However, the Orbiter BLT Tool is not widely applicable to any vehicle configuration or speed regime.

Physics-based models for transition show promise for predicting transition analytically and/or computationally.[2] Such techniques would be more broadly applicable across flight vehicle types and speed regimes. There is a lack of available experimental flowfield data to validate and evaluate physics-based models, particularly in supersonic and hypersonic flows. While many suitable fluid flow visualization and quantitative measurement techniques exist for subsonic flows, supersonic and hypersonic flows present challenges for such instrumentation. Physical probes such as hot wires perturb high Mach number flows, are influenced by shock waves forming on the probes, and are easily damaged in supersonic and hypersonic flow facilities. Particle-based measurement techniques like particle image velocimetry (PIV) and laser Doppler velocimetry (LDV), which work well in subsonic flows, are not readily applicable to supersonic and hypersonic flows, owing to difficulties in providing sufficient amounts of seed material and uniform particle seeding. Particle lag is also a concern in flows with steep velocity gradients. Even non-quantitative flow visualization methods are challenging in supersonic and hypersonic flows. Whereas smoke or fog can easily be introduced and visualized with laser sheets in many subsonic facilities, introducing such seed material in supersonic and

---

hypersonic facilities is more problematic. The schlieren technique provides valuable visualizations in supersonic and hypersonic flow fields, but this method is path-averaged so flow structures cannot always be clearly discerned.

We have recently demonstrated that the nitric oxide planar laser-induced fluorescence (NO PLIF) technique can visualize transitional flow structures in hypersonic flow facilities.[3] In that experiment, a small quantity of pure NO was locally seeded into the flow through pressure ports in the model. The NO mixed with the boundary layer fluid and passed downstream along a flat plate, and over a discrete roughness element designed to trip the flow. A laser sheet excited these NO molecules and their fluorescence was captured on a CCD camera, visualizing planar slices of the flow. This approach has been adopted for the current study to visualize flow over a flat plate without roughness as well as the same plate with a single hemispherical roughness element located downstream of the seeding slot. In subsonic flows, hemispherical roughness has been studied both experimentally[4,5] and computationally.[6] Hemispherical roughness was chosen for the current experiment because the shape has no external corners and is a simple geometry, so it is relatively easier to grid for computational studies than cylinders or triangles, for example. Also, the use of hemispheres allows comparisons with this past work, in which hairpin vortices were found to be the dominant flow structures leading to transition to turbulent flow.

II.   Experiment and Analysis Description

The experiments were performed in the 31-Inch Mach 10 Air Tunnel at NASA Langley Research Center. The test apparatus consisted of three main components: the test article, the wind tunnel facility and the PLIF system. The analysis includes image processing and subsequent rendering in a three-dimensional software environment. These procedures are summarized briefly in this section.

A. Test Article

The test article was a 20° full-angle wedge with a sharp leading edge. Figure 1 shows a computer rendering of the model. The top surface of the wedge is a planar surface, herein referred to as a *flat plate*. The flat plate was 127.0 mm (5 in.) wide and 157.2 mm (6.2 in.) long. This flat plate was oriented at an angle between 5° and 25° with respect to the oncoming flow during the experiments. On this surface, we attached a hemispherical protrusion to trip the flow from laminar to turbulent. The boundary layer trip was attached 75.4 mm (2.97 in) downstream of the sharp leading edge of the model. NO was seeded into the flow through an 11.0 mm (0.43 in) long by 0.81 mm (0.032 in) wide spanwise slot, located on the model centerline, as shown in Fig. 1. The upstream edge of the slot was located 29.4 mm (1.16 in) downstream of the model's leading edge. Thus the end of the flat plate was 128

Figure 1. Test article used in the experiment, showing the assembled wedge model and trip. The model includes the sting, flat plate (top surface), sharp leading-edge, seeding slot insert, and the 2-mm radius hemispherical trip.

mm (5.0 in) downstream of the upstream edge of the slot. Pure NO was supplied through a mass flow controller to a plenum below this slot and the NO then passed through the slot into the flow. Flowrates between 0.03 and 1.0 standard liters per minute (slpm) were used, corresponding to flow velocities issuing from the slot of about 2 to 68 m/s (6.6 to 223 ft/s), depending on the flowrate, model angle of attack (AoA), and tunnel operating conditions. These flow velocities are much lower than the 1,250 m/s (4101 ft/s) flow velocity calculated at the edge of the boundary layer for these conditions. Most of the images were obtained using 0.3 slpm, corresponding to a flow velocity of 20 m/s (65 ft/s) for the $P_0 = 720$ psi condition.

Because one of the primary aims of this study was to study boundary layer transition, it was important that the method of seeding nitric oxide into the flow (which was required for NO PLIF flow visualization) perturb the flow as little as possible, and especially that it not induce turbulence in the flow. The use of a slot for seeding (as opposed to the 4 pressure ports used in Reference 3) and the choice of a flowrate of 0.3 slpm was largely based on the work of Berry et al.[7] who studied blowing-induced transition on a Hyper-X forebody model. Berry et al. found that, for a given flowrate of gas, injection from a spanwise slot was the least effective method and that a spanwise row of holes was the most effective method for tripping a boundary layer to transition to turbulence. Since we wanted to minimize the perturbation to the flow, we selected a spanwise-slot-shaped orifice to seed the NO. Berry et al.'s experiment was performed in this same facility and had remarkably similar conditions to the current experiment: they estimated an edge Mach number of 4.4 and had a unit Reynolds number of 2.2 million/foot. In the present experiment, considering the
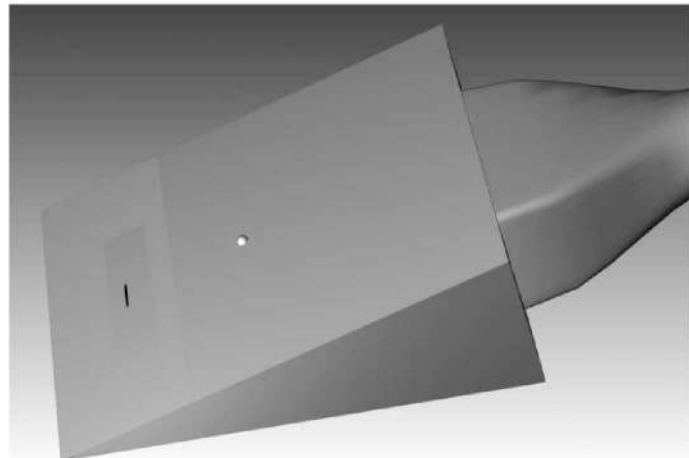
highest Reynolds number flow probed (the worst case regarding transition) the unit Reynolds number was 1.9 million/foot and the edge Mach number was estimated from an oblique shock calculation to be about 4.2 for the 20° flat plate angle of attack case. The distance from the seeding slot to the first compression corner in Berry et al.'s experiment is 127 mm (5.0 in), which is nearly identical to the distance from the seeding slot to the end of the flat plate in the current test. Such similar conditions allow more quantitative comparisons to be made between the present seeding method and those studied by Berry et al. Berry et al. found that injection from the slot could transition the flow in this distance using 0.00032 kg/s (0.0007 lb/s) of flow. In the current experiment, using 0.3 slpm, we supply gas at a 50 times lower mass flowrate, which is much lower than the flowrate required to force the flow to transition. However the length of the slot in Berry et al.'s experiment was 51 mm (2.0 inches) whereas the slot in the current work is only 11 mm (0.43 in) long. Taking into account the mass flow per unit length of the slot, the supplied flow is still 10 times lower than that required to trip the flowfield. Furthermore, since the width of the current slot was 6.4 times larger than the 0.13 mm (0.005 in) slot used by Berry et al, the flow velocity was lower by the same factor of 6.4, which likely would be less perturbing to the flow. Thus, the low flowrates used in this experiment were not expected to transition the flow to turbulence on the model surface.

The composition of the gas in the boundary layer downstream of NO injection can be estimated from the flowrates. Assuming that the NO uniformly mixes through and stays within the boundary layer fluid (air), and considering the mass flowrate of the air in the boundary layer that passes over the slot (boundary layer thickness predicted to be 1.06 mm in Reference 3), the mole fraction of NO downstream of the trip is predicted to be 0.026, the rest being air. This calculation was performed for the $P_0 = 720$ psi condition assuming a 20° flat plate angle of attack and a NO flowrate of 0.3 slpm. For the temperatures and pressures in this computation, the NO chemistry is frozen.[8] Thus, even though pure NO is seeded into the flow, the NO only makes up a very small proportion of the fluid in the boundary layer. Stated another way, seeding NO at these rates very minimally displaces the air in the boundary layer.

The model used in these experiments contained some minor imperfections. The 11 mm long seeding slot was an interchangeable insert (barely visible in Figure 1). Unfortunately, this insert was recessed slightly relative to the plane of the flat plate and consequently presented some small steps and gaps to the oncoming flow. The insert itself was 63.5 mm by 15.9 mm (2.5 in by 0.625 in), oriented with the long dimension in the spanwise direction. The front edge of the seeding slot was 6.1 mm (0.24 in) downstream of the front of the insert. The gaps were sealed with a high temperature RTV silicone, but some notable steps and gaps persisted. Using feeler gauges, the gas seeding insert was measured to be 0.1 mm (0.004 in) below the surface of the flat plate, presenting a slight rearward facing step followed by a similarly sized forward facing step. A 1 mm (0.04 in) deep and 0.25 mm (0.01 in) wide gap was present along the 63.5 mm (2.5 in) length upstream of the gas seeding insert. The gap downstream of the insert was negligible. Furthermore, there were surface imperfections because the model had been painted, some of the paint had been chipped off by particulates from the tunnel, and the model had been repainted several times without completely stripping the paint. Thus, surface roughness on the order of a few layers of paint thickness was randomly distributed around the model. Nonetheless, these surface imperfections were an order of magnitude or smaller than the 2 mm radius trip used to perturb the flow. Despite efforts to measure it, the sharpness of the leading edge could not be quantified. Care was taken to prevent the sharp leading edge from becoming damaged, though slight imperfections to this edge may exist. To first order, the model imperfections described in this paragraph should be negligible, but they could have an effect on higher fidelity computations of the flow.

B. Wind Tunnel, Tunnel Operating Conditions and Data Acquisition

The 31-Inch Mach 10 Air Tunnel is an electrically-heated blowdown facility located at NASA Langley Research Center in Hampton, Virginia, USA. Reference 9 details this facility, a brief summary of which is provided here. The facility has a nominal Mach number of 10 and a 31-inch square test section and operates on electrically heated, compressed air. Large windows, transparent in the ultraviolet down to approximately 190 nm, form three walls (including top and bottom) of the test section with the fourth wall formed by the model injection system. In both experiments, the model was side-mounted to this fourth wall. Run durations for the current tests were about one minute. The nominal stagnation temperature was 1,005 K (1,350° F) for all tests described herein. Two different facility stagnation pressures, P_0, were used: 4.96 MPa (720 psia) and 9.31 MPa (1350 psia). The two operating pressures simulate freestream unit Reynolds numbers of 3.3 million/m and 6.1 million/m (1.0 million/ft and 1.9 million/ft), respectively. Throughout the paper, these two different tunnel operating conditions are referred to simply as the 720 psi condition and the 1350 psi condition. Further details of the flow properties at these conditions can be found in Hollis et al.[10] or can be requested from the authors.

The normal sequence of operation was to begin NO flow prior to beginning a wind tunnel run so the flowrates could establish. Data acquisition was started upon injection of the model into the wind tunnel and image acquisition was then initiated. An output signal from the intensified CCD indicated to the data acquisition system that PLIF image

acquisition had begun. To visualize different locations within the flow, a remote manual translation stage trigger was used to start a sweep of the laser sheet across the model.

C. Planar Laser-Induced Fluorescence (PLIF) Imaging System

The PLIF system consisted primarily of the laser system, beam-forming optics and the dual-camera detection system. The laser system had a Spectra Physics Pro-230 Nd:YAG pump laser, a Quanta Ray PDL-2 tunable pulsed dye laser, and a Quanta Ray WEX wavelength extender, all operating at 10 Hz and with ~10 ns pulse duration. The laser output was tuned to a wavelength of 226.256 nm, chosen to excite the strongly fluorescing spectral lines of NO near the Q_1 branch band head. Lenses formed the laser beam into a sheet, exciting the NO fluorescence. The sheet was about 0.5 mm thick and was diverging slightly to a width of about 150 mm (6 in) to illuminate the model. Images were acquired using a pair of Princeton Instruments PIMAX-2 intensified CCD cameras with 512x512 pixels. The cameras were side-by-side with a slight angular separation (< 15°) so that they both viewed the center of the wedge model. One camera used a Nikon 105 mm focal length, F/4.5 UV Nikkor lens. For electrical timing and triggering reasons, this camera was known as the *master* camera. The other camera used a Cerco 45 mm focal length, F/1.8 UV lens. This camera was known as the *slave* camera. The slave camera was synchronized with the master camera to acquire simultaneous images. Flow visualization images were acquired with a 1 μs camera gate at 10 Hz, in sync with the laser. So-called *dotcards* (a flat card marked with evenly spaced dots) were used to determine image magnification in post-processing and for correcting perspective and lens distortion as in previous work.[11] The camera spatial resolutions were 10.8 pixels/mm for the master and 4.2 pixels/mm for the slave.

By translating the laser sheet, visualization was possible at different locations in the flow, thereby visualizing flow structures that developed and evolved both along and away from a surface. As in prior work, the laser sheet could be oriented either perpendicular to the surface of the model, to obtain a *side view* of the flow, or it could be oriented parallel to the surface of the model, to provide a *plan view* of the flow. In both configurations, the cameras were oriented approximately normal to the laser sheet. For side views, the angle of the model could be varied during a run. However, for plan views, the model angle had to remain fixed. During plan view runs, the laser sheet position and (sometimes) the flowrate were varied during the run. Further details of the mobile NO PLIF system and its use in NASA Langley Research Center's 31-Inch Mach 10 Air Tunnel can be found in Refs. 12 and 13.

D. PLIF Flow Visualization Image Processing

The images presented herein were not smoothed in post-processing but they were processed to correct for the variation in the laser sheet's intensity across the field of view of the camera. Since the laser sheet intensity was not monitored on a shot-to-shot basis, an averaged laser sheet intensity image was obtained by filling the evacuated wind tunnel test section with a low quantity of NO and acquiring a 100-shot averaged image just prior to each tunnel run. The individual single shot images were divided by this averaged image to provide a first order correction. Prior to dividing through by this averaged laser sheet profile, a background image was subtracted from single-shot PLIF images to remove background counts. The lower resolution (slave) images were corrected to remove lens and perspective distortion (see Ref. 11). A false color table was then applied. The color table goes from transparent at very low signal intensities to purple to red to yellow to white as the PLIF intensity increases. These last two steps were not taken with the higher resolution (master) images.

E. Virtual Diagnostics Interface (ViDI)

The Virtual Diagnostics Interface (ViDI)[14] is a software tool, developed at NASA Langley Research Center, that provides unified data handling and interactive three-dimensional display of experimental data and computational predictions. It is a combination of custom-developed software applications and Autodesk® 3ds Max®, a commercially available, CAD-like software package for three-dimensional rendering and animation.[15] ViDI technology can be applied to three main areas: 1) pre-test planning and optimization; 2) visualization and analysis of experimental data and/or computational predictions; and 3) establishment of a central hub to visualize, store and retrieve experimental results. For this experiment, ViDI was used for post-test visualization of the slave PLIF images, which had been processed as described in the previous section. Images were overlaid on the model using dotcard images to ensure proper scaling and orientation. Renderings of the model and the image plane were generated using either of two virtual cameras: one fixed in space and one attached to the model. The latter virtual camera is used for most of the figures in this paper because it removes the distracting motion of the model during angle of attack sweeps.
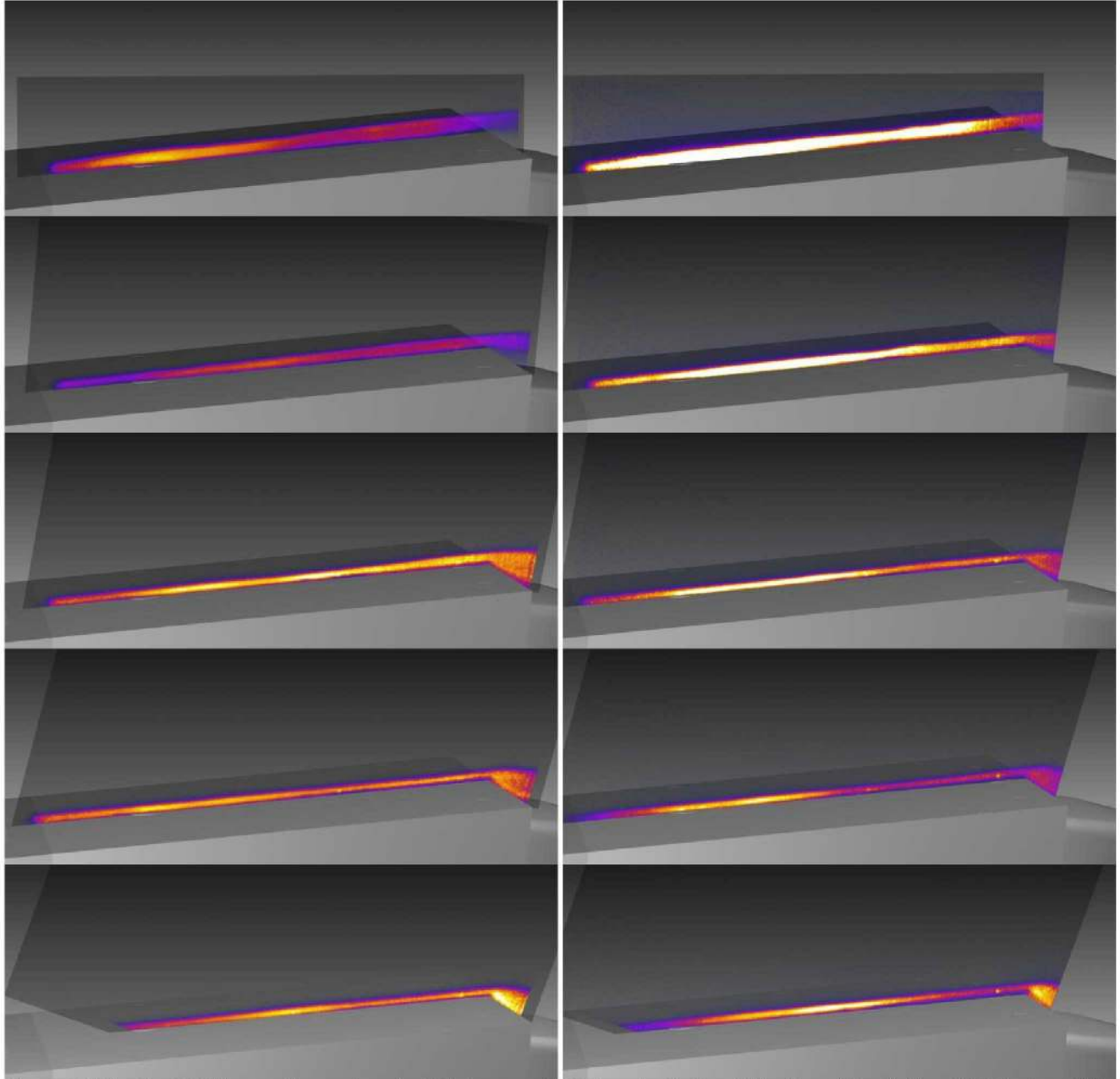
Figure 2. Side view PLIF images for no trip using NO flowrate of 0.3 slpm for the P_0 = 720 psi condition (left) and 1350 psi condition (right). From top to bottom the flat plate angles with respect to the flow is: 5°, 10°, 15°, 20°, 25° (+/- 0.5°). Flow is from left to right.

Results

A. Flow over the flat plate with no trip

1. No trip: Side views

Before studying flow over discrete roughness elements, it is important to understand the flow in the absence of the trips. Hypersonic laminar boundary layers are relatively well understood but seeding with NO by injection through a slot can potentially perturb this laminar flow. Ideally, the flowfield produced should be laminar and free from streaks or vortices. Since NO was being seeded into the flow, a primary concern was to see whether the flow of NO was changing the boundary layer thickness or forcing the flow to transition to turbulence. Based on our prior work,[3] flow conditions of P_0 = 720 psi, flat plate AoA = 20° and an NO flowrate of 0.3 slpm was determined to be the nominal starting condition for current work for the following reasons: this combination of AoA and P_0 produced transitional flow

structures on the test article and the flowrate provided sufficient NO to generate good quality PLIF images. In the present study, we wished to vary these parameters to study the resulting image and flow quality in the absence of trips to determine the suitability of these conditions. Both side views and plan (top) views were obtained and the laser sheet position, as well as AoA, P_0, and NO flowrate were varied and measured, as shown in Figs. 2-7.

Figure 2 shows NO PLIF images obtained with the same flowrate (0.3 slpm) and two different tunnel stagnation pressures (720 psi and 1350 psi) while varying the angle of attack. The angle of the model does not appear to change because the renderings were created from a virtual camera that was attached to the reference frame of the model in the computer visualization software. The use of this virtual camera allows the growth of the boundary layer to be more readily apparent as the angle of the plate decreases with respect the flow.

Initial observation of these images shows smooth laminar flow, but with gradual left-to-right variations in brightness (color) such as in the top-left image. This left-to-right variation is caused by imperfect correction of the laser sheet intensity and should be ignored. In the direction normal to the flat plate, the PLIF intensity is seen to be very low at the wall, increasing to a constant level inside the boundary layer and then suddenly dropping off. Below, we will substantiate that this outer edge corresponds approximately to the same height as the boundary layer thickness, δ, based on the total enthalpy. Thus, the NO is seeding the boundary layer fluid only. The edge of this boundary layer does not make a perfectly smooth arc as it propagates downstream: some degree of wavy curvature, indicating unsteadiness, is observed in these images, though these are much smoother than the transitional structures to be shown below.

As the flat plate is brought more parallel to the freestream, the boundary layer thickens, owing to the increase in edge Mach number and the corresponding decrease in gas pressure near the surface. This thickening of the boundary layer occurs in both $P_0 = 720$ and 1350 psi cases. Though it is difficult to immediately see from these images, the 1350 psi case has a slightly thinner boundary layer than the 720 psi case, as expected, because of the factor of 2 higher pressure and Reynolds number. To the right side of the plate, in most cases, the images capture the separated flowfield over the rearward facing step downstream of the flat plate. As the plate becomes more parallel to the freestream flow, the pressure on the surface of the flat plate drops and the turning angle of this flow separation decreases.

As in our past work,[3] we have measured the boundary layer thickness from the PLIF images. This was done for two reasons: to compare the magnitude of the boundary layer thickness deduced from the images with more conventional measures from CFD (e.g., thickness based on velocity or enthalpy profile) and to investigate the effect of seeding. Of primary interest was to determine whether seeding NO thickened or otherwise perturbed the boundary layer. The method of measuring the boundary layer thickness from the PLIF images was previously developed in Reference 3. The magnification (in pixels/mm or pixels/in) of the images was determined from images of dotcards. Then profiles of PLIF intensity distribution normal to the flat plate were selected in individual images. The PLIF boundary layer thickness was determined from the distance between the two points in this profile having 50% of the maximum signal intensity. This convention is known as the full width at half maximum (FWHM).[3] We chose to make this measurement at the location corresponding to where the trips were placed in other runs. However, trips were not inserted into the flat plat for the images studied in this section. For each measurement, at least five separate images were sampled and the resulting boundary layer thicknesses were averaged. Based on these measurements, three quantitative comparisons could be made: the variation of PLIF boundary layer thickness with AoA, the variation of PLIF boundary layer thickness with NO flowrate and the variation of boundary layer thickness with Reynolds number (proportional to the tunnel stagnation pressure, P_0), all else being held constant.

Figure 3 shows the variation of the boundary layer thickness as the angle of attack of the flat plate is changed. This experiment was performed with $P_0 = 720$ psi and the NO flowrate held constant at 0.3 slpm. The boundary layer thickness based on the PLIF measurement is observed to increase by a factor of 2.6 between the 25° and the 5° flat plate AoA. This is the same trend as observed visually in Fig. 2. When the higher-resolution master camera was used to determine the boundary layer thickness the error bars were much smaller compared to the slave camera. The magnification of the master camera was 2.6 times higher than the slave camera. However, the master camera could not be used for all measurements because the flat plate left the field of view of the camera for angles less than 16°. While the master camera images were well focused and exhibited only 2 pixels (corresponding to 0.2 mm or 0.009 in) of blurring, the larger aperture slave camera was less focused and showed over 4 pixels (1 mm or 0.04 in) of blurring, as well as blooming from the intensifier (additional blurring of ~2 pixels in the brightest parts of the images). These measurement artifacts increased the size of the error bars for the slave camera images. These blurring phenomena were deconvolved from the data shown in the figures, assuming that the blurring and the true boundary layer thickness add in quadrature. The assumed blurring in the slave camera was adjusted within reasonable limits so that the data point at 15° flat plate angle would continue the trend of the data obtained using the master camera.
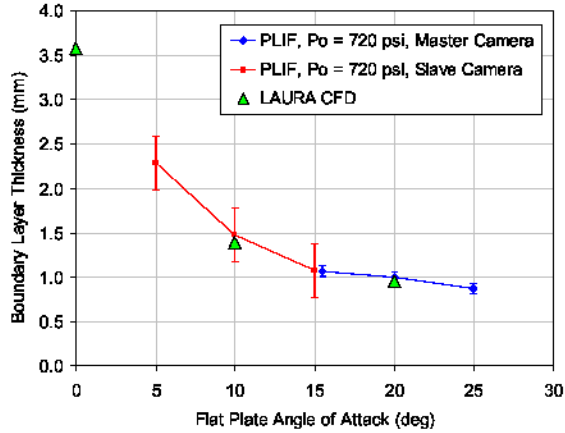
Figure 3. Boundary layer thickness based on NO PLIF intensity distribution normal to the flat plate and CFD, at the trip location (though no trip was present for this run).

Also shown in Fig. 3 is the boundary layer thickness from a LAURA (Langley Aerothermodynamic Upwind Relaxation Algorithm) computational fluid dynamics (CFD) simulation of this flat plate flow, computed for Ref. 3, but considering the position of the trip in the current experiment. The boundary layer thickness shown from CFD is defined as the location where the total enthalpy is 99.5% of its free-stream value.[3] Clearly this is a different criteria than used to determine the PLIF boundary layer thickness. Unexpectedly, these two measures of boundary layer thickness coincide within the experimental uncertainty. In Ref. 3, a larger discrepancy – typically 0.5 mm or 0.02 in – was observed. In that comparison, the blurring was not deconvolved from the PLIF thickness, though the blurring was probably not large enough to account for the discrepancy in Ref. 3. Nonetheless, the boundary layer thickness based on the PLIF measurements appears to closely track the more conventional CFD-based thickness prediction based on the flow enthalpy.

Figure 4 shows how the boundary layer thickness changed with NO flowrate. For the $P_0 = 720$ psi case, the boundary layer thickness remained constant, within experimental uncertainty, while the flowrate was increased by more than a factor of three. But when the flowrate was increased by another factor of 3, to >1 slpm, we observed a boundary layer thickness increase of 18% compared to the earlier cases. For comparison, we estimate that the mass addition to the boundary layer from the NO seeding is 2.6% for the 0.3 slpm case and 10% for the 1 slpm case.
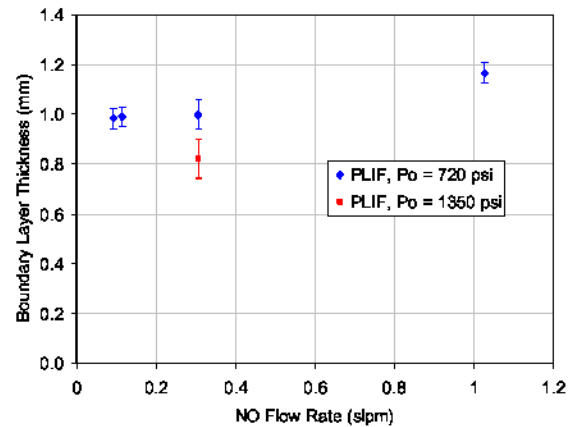
Based on these observations, the choice of 0.3 slpm for the NO flowrate in the subsequent imaging experiments seems justified based on the desire to minimally increase the boundary layer thickness. Also shown in Fig. 4 is the measured boundary layer thickness for the higher Reynolds number run which had a 1350 psi stagnation pressure, which is smaller than for the 720 psi case, as expected.

2. No trip: Plan views

To further investigate flow structures present in the boundary layer, the model was rotated and the laser sheet and cameras were repositioned the so that plan views of the flow

Figure 4. Boundary layer thickness based on NO PLIF intensity distribution normal to the flat plate at the trip location (though no trip was present for this run).

could be obtained. Figure 5 shows some of the resulting images obtained at the 720 psi stagnation pressure condition. The left column of images was obtained using 0.03 slpm flowrate of NO while the right-hand column used 0.3 slpm of NO. Though hundreds of images were obtained, only three images are shown for each flowrate. These were chosen to be representative of the data set. The three images shown for each flowrate were obtained at different heights above the surface of the flat plate. The measurement location was changed by attaching the sheet-forming optics to a stepper motor and moving the stepper motor during the run. The legend in the top left-hand corner indicates the approximate laser sheet position, which was monitored using a string potentiometer attached to the sheet forming optics. Unfortunately, vibrations of the model and the sheet-forming optics caused the laser sheet to fluctuate randomly up to 1 mm (0.04 in) relative to the model surface during the tunnel runs, so the sheet position indicator is approximate. The model also changed its mean position during the runs, possibly due to heating or loading, further complicating interpretation of the location of the images above the model surface. In some cases, surface features such as scattered light from surface roughness on the model, or scattered light from the trip itself allowed for the laser sheet position to be accurately determined. Such positions could be used as calibration points to correct for the relative position of the laser sheet with respect to the model. However, random fluctuations were difficult or impossible to correct. If accurate boundary layer thickness information is required, then side views of the model and flow, as shown in Fig. 2, can provide that information. Alternately, a thick laser sheet, possibly combined with stereoscopic imaging can be used to capture the entire boundary layer flow.[16]

Most of the PLIF images obtained with a 0.03 slpm flowrate showed streamwise streaks similar to those seen in all images in the left-hand column of Fig. 5. When the flowrate was increased by a factor of 10 to 0.3 slpm, the streamwise streaks became much less apparent and less frequent. At the outer edge of the boundary layer (see the top-right image

7

American Institute of Aeronautics and Astronautics

of Fig. 5), some streaks were still observed. However, closer to the model surface, in the center of the boundary layer, the streaks seemed to be suppressed by the flow of NO.

Figure 6 shows a similar progression of increasing NO flowrates but for the 1350 psi stagnation pressure condition. Three images are shown for each of four different NO flowrates. Again the groupings of three images show different heights of the laser sheet above the surface of the model. For the 0.02 slpm and 0.1 slpm case, streamwise streaks are observed. Again the 0.3 slpm case shows reduced streaks in most of the images closest to the model surface. Further above the model surface, near the edge of the boundary layer, streaks were observed in most images regardless of flowrate. For the highest flowrate of 1.0 slpm, the images close to the surface of the model are relatively smooth and free of streaks, though the fluorescence is observed to attenuate from top to bottom in the images. This attenuation is in the direction of the laser sheet propagation. It is caused by absorption of the laser sheet energy by the high NO concentration. This absorption artifact is undesirable in the images because it further complicates their interpretation. For the 1 slpm flowrate, a few of the images showed corkscrew shaped streamwise structures, possibly vortices, near the edge of the boundary layer. One of these images is shown in Fig. 6. If these corkscrew shaped structures are caused by the high NO flowrate seeding, then this is clearly an undesirable perturbation. Figure 7 shows diagonal flow nonuniformities observed most frequently when the NO flowrate was 1.0 slpm. The position of these streaks on the flat plate was not repeatable, suggesting that they are non-stationary. For the 1.0 slpm flowrate, the diagonal streaks occurred in about 15% of the images obtained, whereas for lower flowrates they occurred less than 1% of the time. An additional consideration is the signal-to-noise ratio in the images. The signal-to-noise ratio increases with NO flowrate as can be observed in Fig. 6 where the lower flowrate images have a more grainy appearance. (The signal-to-noise ratio can best be judged by the graininess of the images since the images were re-scaled arbitrarily during image processing so that the maximum signal intensity during the scan approaches a yellow-white color.) Thus the highest flowrate of NO that does not perturb the flow or otherwise introduce undesirable artifacts was desired. Based on these considerations, a flowrate 0.3 slpm was used in the remainder of the work, for both 720 psi and 1350 psi stagnation pressure conditions.
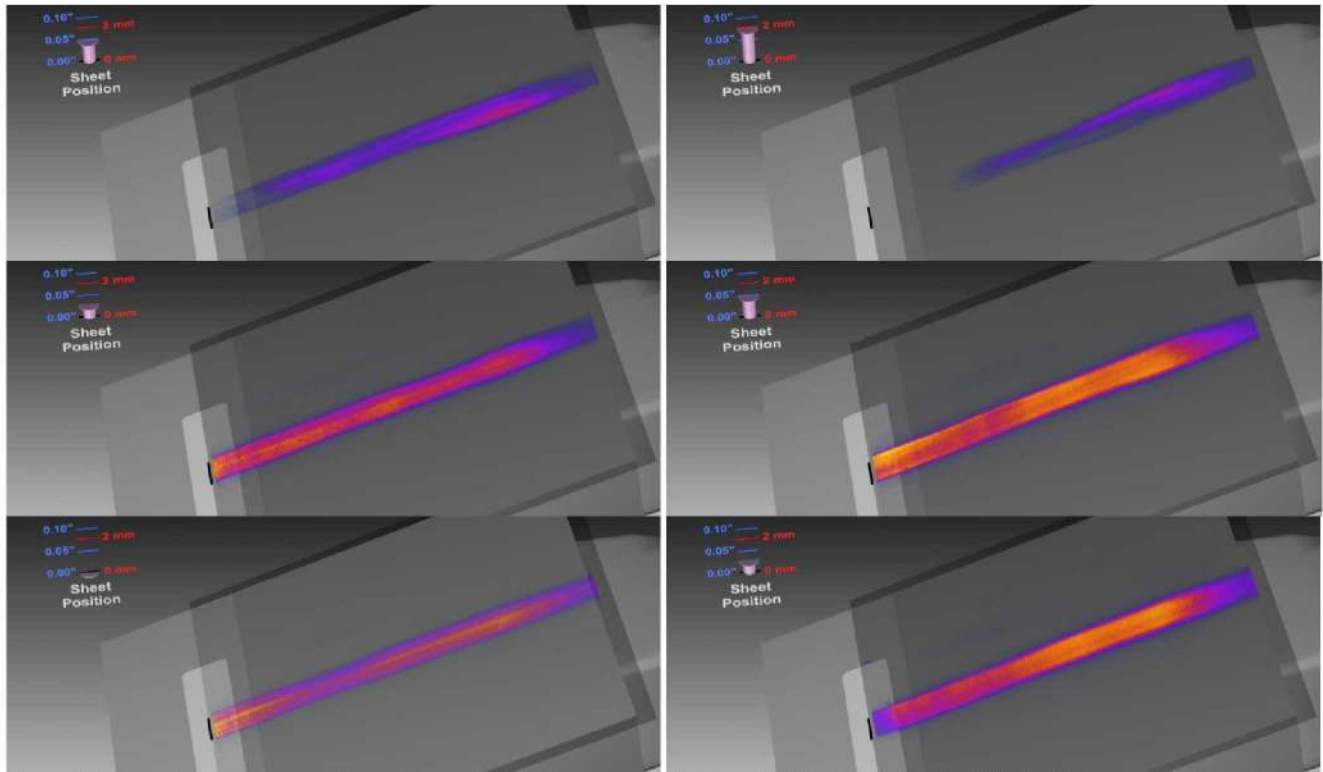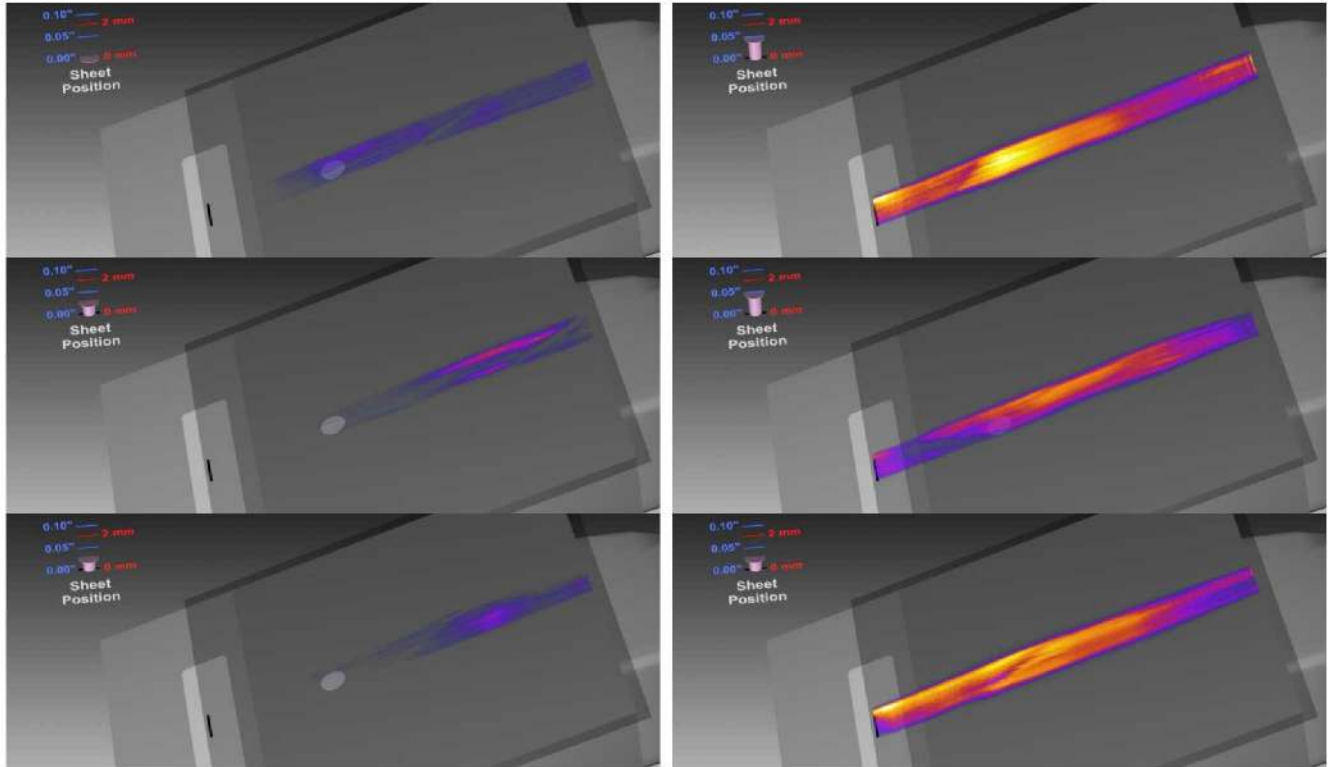

Figure 5. Plan view PLIF images for no trip, with NO flowrates of 0.03 slpm (left) and 0.3 slpm (right), for the $P_0 = 720$ psi condition. Flow is from left to right.
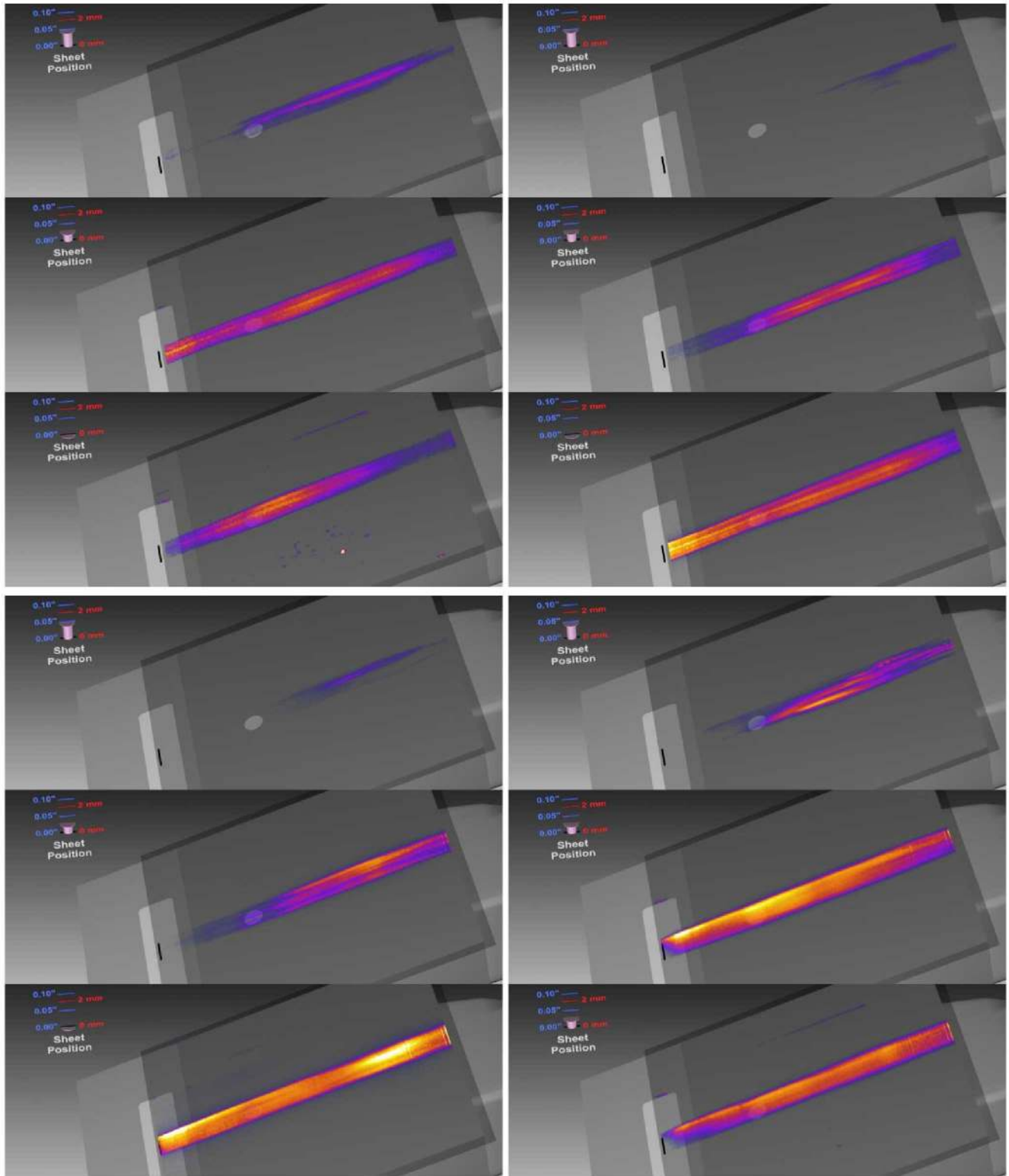
Figure 6. Plan view PLIF images for no trip, with NO flowrates of 0.02 slpm (top-left three panels), 0.1 slpm (top-right three panels), 0.3 slpm (bottom-left three panels) and 1.0 slpm (bottom-right three panels) for P_0 = 1350 psi.

Figure 7. Plan view PLIF images showing diagonal instabilities for P_0 = 1350 psi, and an NO flowrate of 0.3 slpm (left) and 1.0 slpm (right).

3. No trip: Pressure measurements

Analysis of pressure measurements can also help in understanding the influence of the NO seeding and possible perturbation to the flow field. A 0.76 mm (0.03 in) diameter pressure tap was installed normal to the surface of the plate and was located 33.3 mm (1.31 in) downstream of the leading edge and 23.1 mm (0.91 in) from the side of the plate. This tap measured the static pressure on the surface of the flat plate (plate pressure) while another identical pressure sensor determined the pressure inside the NO seeding chamber (plenum pressure) with an accuracy of 14 Pa (0.002 psi). Long tubes connected the pressure sensors to the measurement locations, resulting in a time lag of 1-2 seconds in the measurements, with faster response times when higher pressures were being measured. Figure 8 shows these two pressure measurements as a function of angle of attack for an angle of attack sweep.

As the flat plate angle is increased, the static pressure on the surface of the flat plate increases. The plenum pressure must increase in concert with the static pressure on the flat plate in order to maintain a constant flowrate through the seeding slot. In fact, the plenum pressure is higher than the plate pressure by nearly a constant value. Recall that a mass flow controller is supplying gas to the plenum at whatever pressure is required to deliver the set mass flowrate. The red and blue curves show the measured pressures obtained during a continuous AoA sweep from 25° to 5°. The larger filled symbols show pressure measurements obtained by averaging over two seconds of data after discrete changes in the model's AoA, two seconds after the model came to rest. Because the red and blue curves were obtained during an AoA sweep, they show significant hysteresis, caused by the time response of the instrumentation. This is readily observable at the 5° flat plate angle at the end of the sweep; the curves indicate that after the model had come to rest at 5°, the measured pressure continued to decrease slightly, until settling at the same value measured with the model in a fixed position. Also shown in the figure is a theoretical prediction of the static pressure on the surface of the flat
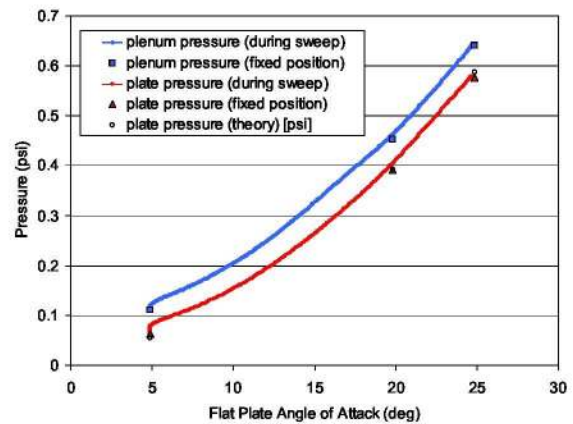
Figure 8 Pressure in the NO seeding chamber (*plenum pressure*) and on the surface of the flat plate (*plate pressure*) during an angle of attack sweep for a P_0 = 720 psi run with an NO flowrate of 0.3 slpm.

plate. This is based upon the free stream pressure processed by an oblique shockwave, neglecting viscous effects. The observed and theoretical surface pressures agree.

The ratio of the plenum pressure to plate pressure is a relevant parameter in the current experiment. Berry et al.[7] found that, for slot injection, the plenum pressure needed to be 25 times higher than the plate pressure to transition the flow to turbulence within 127 mm (5.0 in) of the slot. From the data shown in Fig. 5, the ratio varies from 1.8 to 1.1 as the flat plate angle is changed from 5° to 25°. These pressure ratios are more than an order of magnitude lower than that required to cause transition according to Berry et al. This once again suggests that the seeding method is non-perturbative.

While a pressure ratio of 1.1 across the slot indicates that the flow is subsonic through the slot, a pressure ratio of 1.8 and is nearly high enough to produce choked flow through the hole. Pressure ratios much larger than 2 across the slot would produce an under expanded flow that would protrude out into the flow, possibly perturbing it. In future tests at lower angles of attack (say 0 to 10°), lower flowrates of NO should be used to minimize this perturbation to the flow. Also, the flow of gas out of the seeding slot should be visualized using the PLIF technique to see the resulting jet of gas. This was not done in the current experiment. Nonetheless, most of the images shown in this paper were obtained with a 20° flat plate angle of attack, in which the pressure ratio across the model was only 1.2.

B. Flow over a hemispherical roughness element

1. Side views

The hemispherical roughness element was installed on the surface of the flat plate and three tunnel runs were performed, all using a 0.3 slpm mass flowrate of NO. Figure 9 shows side view images acquired for a run with P_0 = 1350 psi. The images show the laser sheet positioned as close as possible to the centerline of the hemispherical trip while the angle of attack was swept. The top image was obtained with the flat plate most parallel to the freestream, resulting in the thickest boundary layer. This boundary layer appears to be taller than the trip. This image shows a mostly laminar flow developing unsteadiness near the end of the flat plate. At the 10° angle of attack, the unsteady flow structures have propagated closer to the trip and more complicated transitional structures appear to the right side of the image. At a 15° angle of attack, the irregular structures have propagated much further forward and have grown in height compared to the earlier images. These trends continue as the flat plate reaches a steeper angle, with the highest two angles of attack showing more vigorous transitional and perhaps even turbulent flow structures originating at or close to the trip.
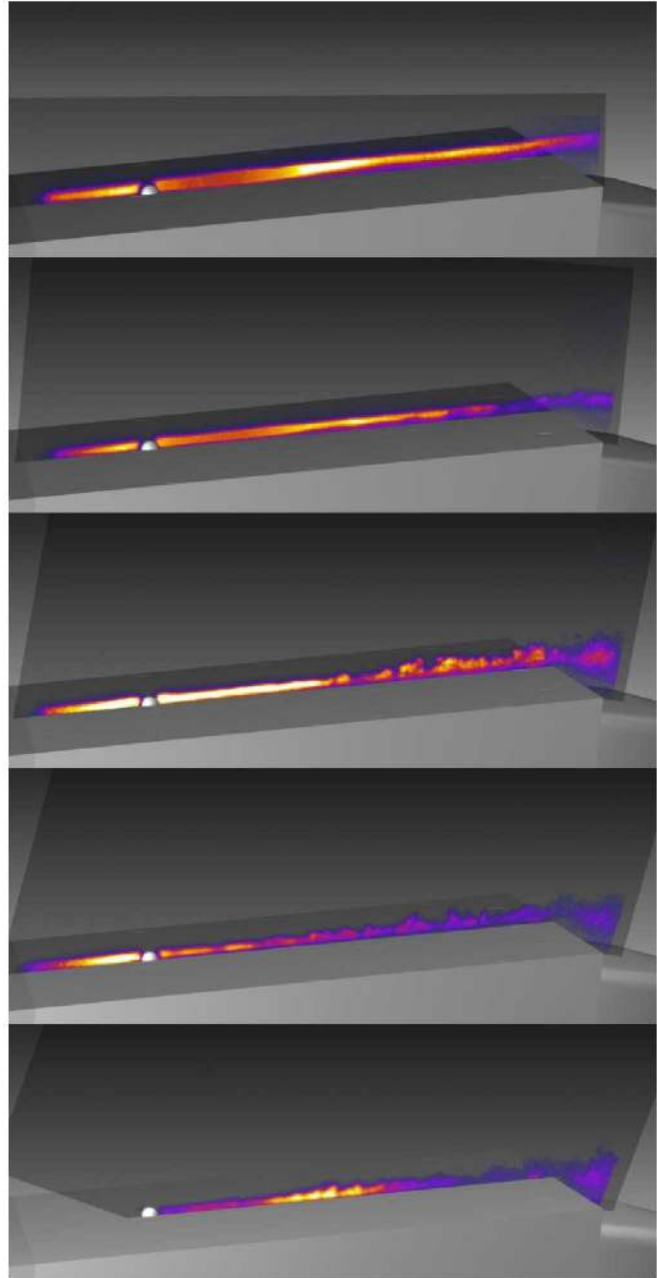
Figure 9. Side view PLIF images of flow over the 2-mm radius hemispherical trip for P_0 = 1350 psi, with an NO flowrate of 0.3 slpm. From top to bottom the images show flat plate angles of attack equal to 5°, 10°, 15°, 20°, 25° (+/- 0.5°).
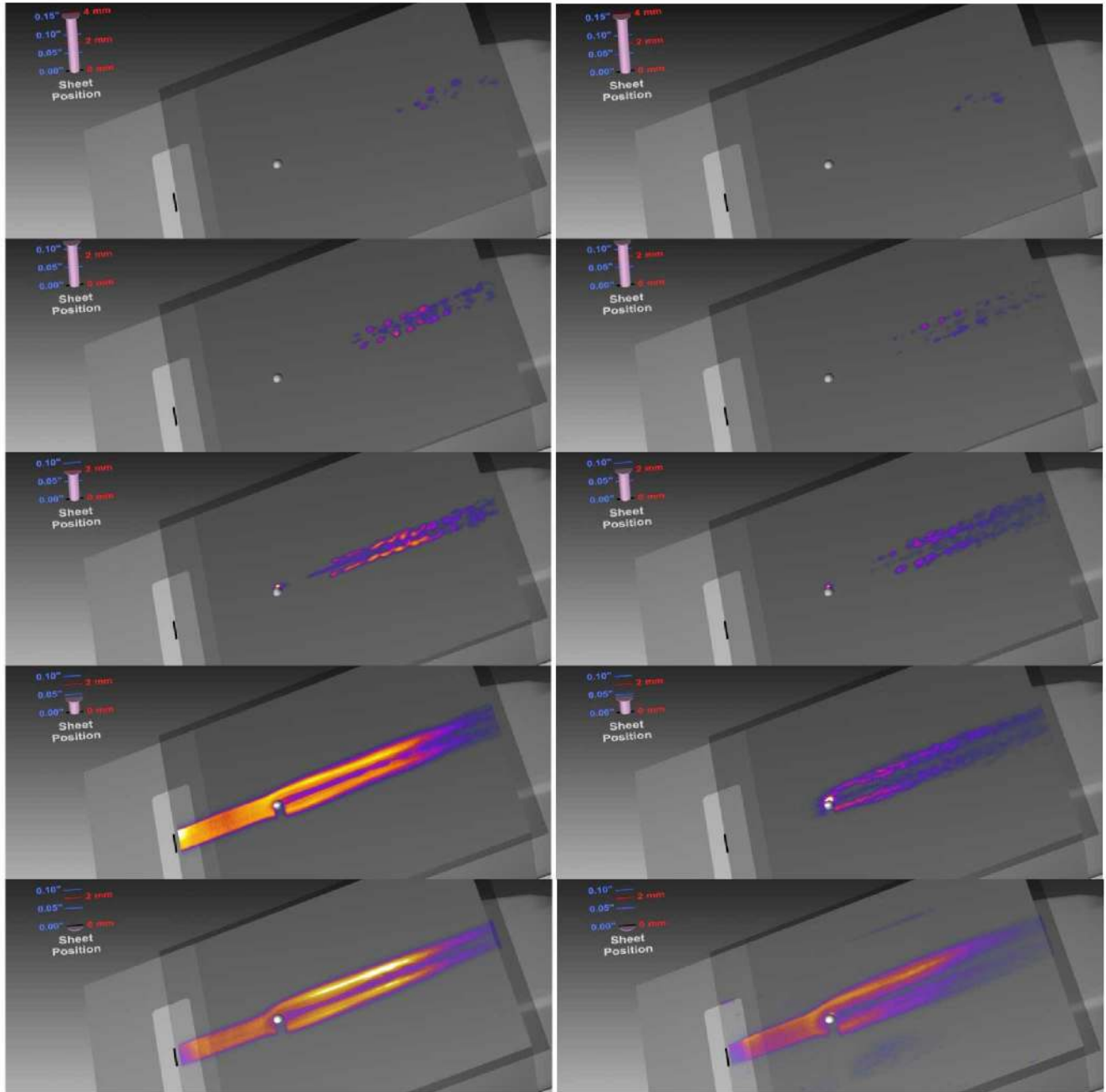
Figure 10. Plan view PLIF images for flow over the 2-mm radius hemispherical trip, for a flat plate angle of 20° and 5 different laser sheet positions. Images shown are from runs where $P_0 = 720$ psi (left-hand column) and $P_0 = 1350$ psi (right hand column).

2. Plan views

Figure 10 shows plan views of flow over the hemispherical trip obtained on subsequent runs. The images in the right-hand column were obtained with the 1350 psi stagnation pressure, similar to the conditions in Fig. 9. The left-hand column in Fig. 10 shows measurements obtained using the 720 psi stagnation pressure condition. Five different laser sheet positions are shown for each run. The bottom row of images in Fig. 10, obtained at or very close to the surface of the plate, show that the incoming stream of fluid is diverted around the sides of the trip. These images acquired at the surface are more smooth in appearance than the images acquired off surface, perhaps indicating more laminar flow along the surface. Measurements obtained about 1 mm above the surface of the plate show a clear wake structure. This wake structure, evident from the lack of seeded NO directly downstream of the trip, oscillates in an organized fashion. Further above the surface, three distinct streaks are observed downstream of the trip. The two outer

12

American Institute of Aeronautics and Astronautics

streaks are streamwise corkscrew-like structures of opposite sign (direction of rotation). The streak in the middle also shows unsteady behavior, which is not necessarily vortical. Even further above the surface, small periodic circular patches of fluid penetrate up into the laser sheet. These are slices through the tops of the corkscrew shaped structures imaged closer to the plate. This 2 mm tall trip is deflecting the ~1 mm thick laminar boundary layer 3 or 4 mm above the surface, but only well downstream of the trip where the laminar boundary layer would have been ~1.3 mm thick. The 1350 psi stagnation pressure run shows smaller scale structures than the 720 psi case, as expected for this higher-Reynolds number flow. Also, the three streaks downstream of the trip are spaced further apart in the 1350 psi case.
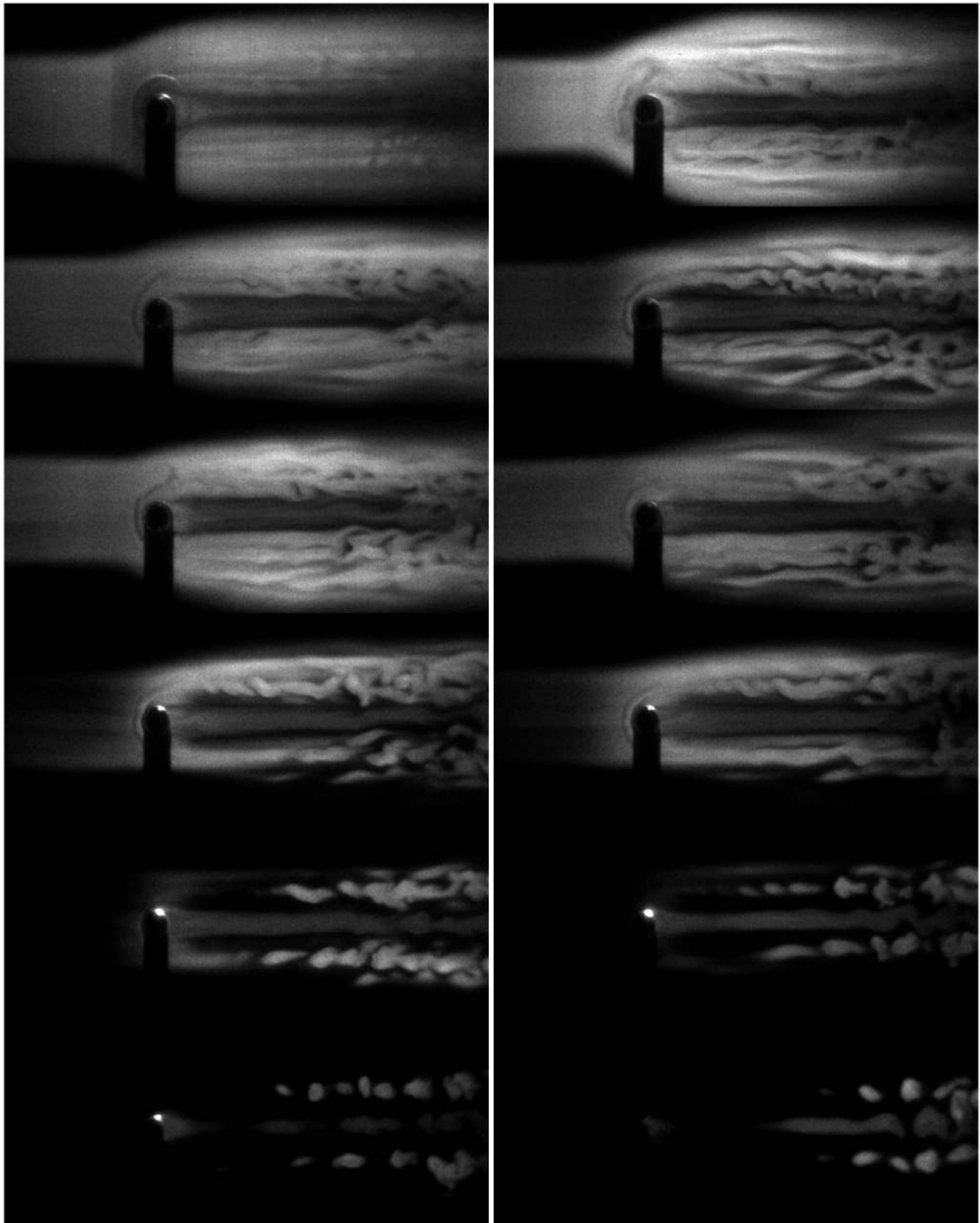
C. Detailed images

Additional insights can be drawn by examining higher-resolution images of the flow. These images were obtained with the master camera, which had a 2.6 times higher magnification than the slave camera images shown above. Higher resolution came at the expense of a smaller field of view. Figure 11 shows images obtained in the same 720 psi run used to provide the images shown in the left column of Fig. 10. The images are shown in approximate sequence of closer to the surface (top) to further from the surface (bottom). The linear grayscale color table was adjusted subjectively to highlight the flow features as clearly as possible. The laser passes from the top to the bottom of the images, and a shadow can be seen below the trip in each image. There is no distinction between the two columns of data – they were all obtained with the same fluid mechanical conditions.

These higher-resolution images clearly show a arc-shaped structure forming just in front of the trip. This appears to be a stationary, or standing horseshoe vortex.[4] In some images, the leading edge of this vortex has a smooth arc shape, while in others it has an irregular or corrugated shape. The top left image, obtained closest to the surface of the plate, does not show the vortex, perhaps because the vortex is located slightly above the surface. Further out, most of the images show the vortex, provided that NO is present to visualize it. Downstream of the trip, these images show significantly more detail than the previous images. For example, the structure and breakdown of the non-corkscrew-shaped unsteady streak along the centerline can be more clearly seen, such as in the two bottommost images in the right-hand column. Also, the images in the second-from-the-bottom row show *five* streamwise streaks instead of three, though the three inner streaks still dominate the images. The corkscrew-shaped structures downstream of the trip are also shown much more clearly in these images. The breakdown of these laminar, streamwise structures (possibly vortices) into more irregular structures is seen in many of the images. Also, some images show as many as 8 different streaks appearing downstream of the trip, for example in the right hand image in the second row from the top.

Images from the higher stagnation pressure run, shown in Fig. 12, also show the absence of the horseshoe vortex very close to the plate (top left image) and the presence of a vortex in front of the trip in the images obtained further off the surface. They show multiple rows of corkscrew-shaped streaks downstream of the trip, similar to Fig. 11. However, they also show more evidence of streaks in the fluid *upstream* of the trip. As expected, the flow structures are smaller in Fig. 12. The streamwise corkscrew-shaped structures are more tightly wound in this case: many more rotations occur in the same distance in the image, when compared to Fig. 11. Flow on the right hand side of the images in Fig. 12 looks much more disorganized than in Fig. 11, implying a further degree of transition to turbulence.

In both runs, the dominant mechanism for laminar-to-turbulent transition appears to be from the counter-rotating, streamwise, corkscrew-shaped structures emanating from the sides of the trip. Previous investigations have shown the presence of so-called *hairpin* vortices, observed experimentally[4] and predicted computationally,[6] for incompressible flow over a discrete hemispherical roughness element. We do not observe these hairpin vortices in the current work. There are notable differences between the current and the past work. First, the current work is a supersonic flow whereas the past work was incompressible. Second, the ratio of trip height to boundary layer in the past work was approximately unity. In the current work, the angle of attack sweep allowed boundary layers both larger and smaller than the trip height to be investigated, but most of the work occurred for the boundary layer approximately half the height of the trip. A third difference is that the PLIF flow visualization method cannot sense the gas flow outside the originally-tagged boundary layer fluid, whereas in prior experimental work, the visualization methods used could probe the fluid outside of the boundary layer. It is possible that hairpin vortices exist in this fluid further from the boundary layer. However this is unlikely because the observed structures do not resemble the near-surface structures seen with hairpin vortices. Future work could investigate smaller hemispherical trip heights to more closely replicate the ratio of boundary layer thickness to trip height in past work to determine whether hairpin vortices are present and can be observed in supersonic or hypersonic boundary layer flow. In hypersonic flow, pairs of streamwise vortices have been observed downstream of discrete roughness elements, such as pizza-box vortex generators by Berry et al, and others.[17] The presence of these vortices was detected by surface techniques – oil flow and phosphor thermography heating.

Figure 11. Detailed plan view PLIF images for flow over the 2-mm radius hemispherical trip for the $P_0 = 720$ psi run at different laser sheet positions. Images at the top of the figure were obtained with the laser sheet located closer to the surface of the plate. The width of these images is 47 mm (1.9 in).

American Institute of Aeronautics and Astronautics
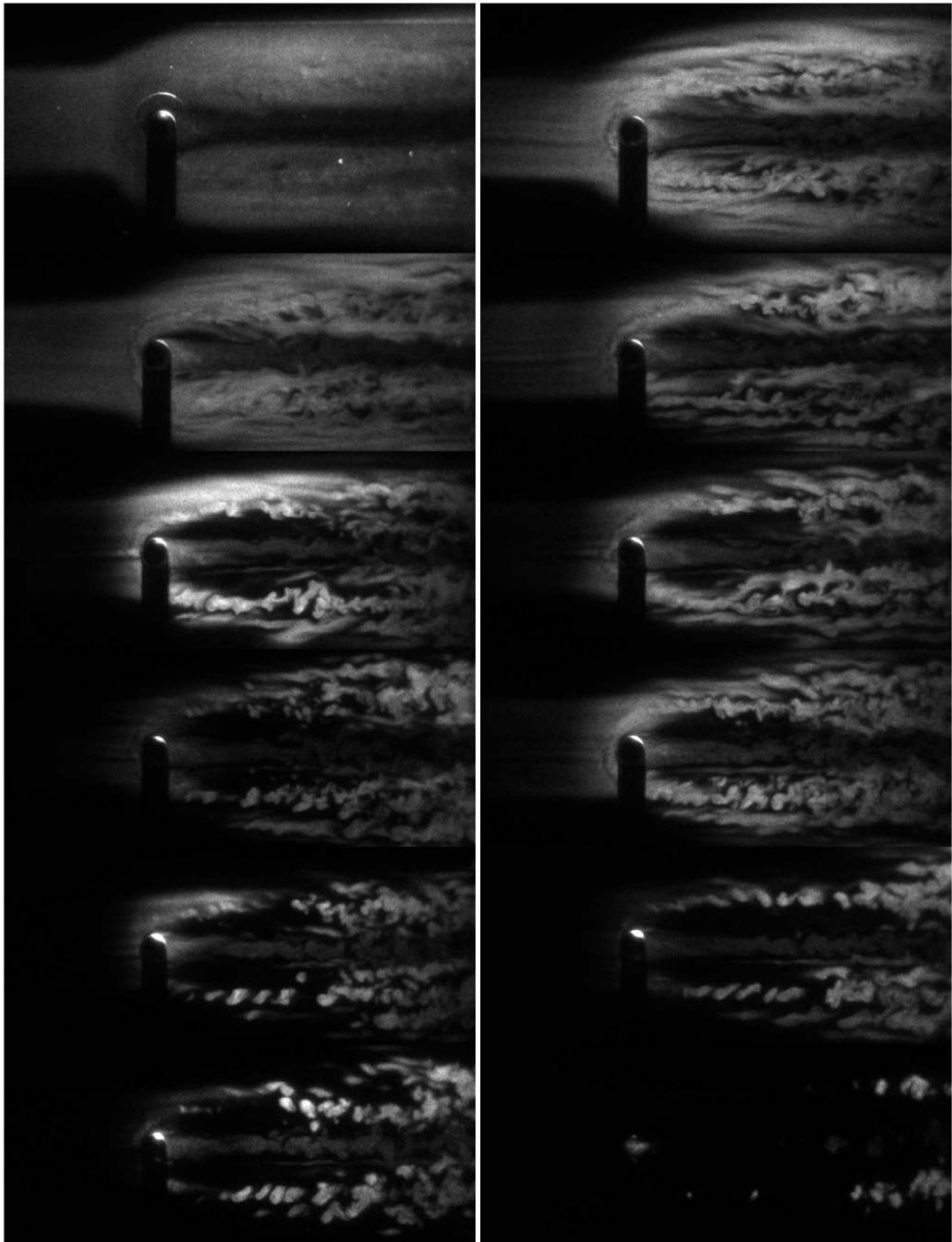
Figure 12. Detailed plan view PLIF images for flow over the 2-mm radius hemispherical trip for the $P_0 = 1350$ psi run at different laser sheet positions. Images at the top of the figure were obtained with the laser sheet located closer to the surface of the plate. The width of these images is 47 mm (1.9 in).

American Institute of Aeronautics and Astronautics

III. Conclusion

In conclusion, the NO PLIF flow visualization method has been used to characterize the laminar flow over a flat plate and a flat plate with a hemispherical roughness element in a Mach 10 flow. Different flowrates of the seeded NO were investigated, with a goal of maximizing image quality while minimizing perturbation to the flowfield. The optimal flowrate of NO of 0.3 slpm provided good signal-to-noise ratio images, while reducing occurrences of streamwise and diagonal streaks, which were observed when using other flowrates. This flowrate also did not increase the visible boundary layer thickness appreciably compared to lower flowrates. By comparing with prior work, the flowrates and pressures used were found to be an order of magnitude lower than those required to force measurable transition to turbulent flow on a similar model. Boundary layer thicknesses determined from the PLIF images agreed with boundary layer thicknesses based on boundary layer enthalpy profiles computed from a CFD code. When the hemispherical roughness element was attached to the flat plate, side view images showed that the flow became increasingly unsteady and tended towards turbulence as the angle of incidence of the flat plate was increased with respect to the oncoming the flow. Plan view images showed numerous rows of cork-screw-shaped structures, possibly vortices, downstream and to the sides of the trip and mostly oriented in the streamwise direction. These structures broke down into more irregularly shaped structures even further downstream. Directly downstream of the trip, a streak was often observed but this streak did not show a corkscrew-shaped structure. Hairpin vortex structures previously observed by others in subsonic flow over a hemispherical trip were not observed in the current experiment. Instead, the streamwise corkscrew-shaped structures appeared to be the leading mechanism for transition to turbulence in this flow field.

Acknowledgments

References

1 S. A. Berry, T. J. Horvath, A. M. Cassady, B. S. Kirk, K.C. Wang, and A. J. Hyatt, "Boundary Layer Transition Results From STS-114," 9th AIAA/ASME Joint Thermophysics and Heat Transfer Conference, AIAA-2006-2922, June, 2006.

2 C-L Chang, M. Choudhari, "Boundary-Layer Receptivity and Integrated Transition Prediction" AIAA Paper 2005-0526, 43rd AIAA Aerospace Sciences Meeting and Exhibit, Reno, NV, January 2005.

3 P.M. Danehy, A.P. Garcia, S. Borg, A.A. Dyakonov, S.A. Berry, J.A. Wilkes Inman, D.W. Alderfer, "Fluorescence visualization of hypersonic flow past triangular and rectangular boundary-layer trips", AIAA-2007-0536, 45th AIAA Aerospace Sciences Meeting, Reno Nevada, January 8-11 (2007).

4 M. S. Acarlar and C. R. Smith, "A study of hairpin vortices in a laminar boundary layer. Part 1. Hairpin vortices generated by a hemisphere protuberance," Journal of Fluid Mechanics Digital Archive, Volume 175, pp 1-41, February 1987.

5 P.S. Klebanoff, W.G Cleveland, K.D. Tidstrom, "On the evolution of a turbulent boundary-layer induced by a 3-dimensional roughness element," J. Fluid Mech., v. 237, pp 101-187, Apr. 1992.

6 H. M. Tufo, P. F. Fischer, M. E. Papka and K. Blom, "Numerical simulation and immersive visualization of hairpin vortices," in Supercomputing '99: Proceedings of the 1999 ACM/IEEE conference on Supercomputing (CDROM), Portland, Oregon, United States, 1999.

7 S. A. Berry, R. J. Nowak, and T. J. Horvath, "Boundary Layer Control for Hypersonic Airbreathing Vehicles," AIAA Paper Number 2004-2246, 34th AIAA Fluid Dynamics Conference and Exhibit, June 28 – July 1, 2004, Portland, Oregon, 2004.

8 J. Olbregts, "Termolecular reaction of nitrogen monoxide and oxygen: A still unsolved problem," International Journal of Chemical Kinetics, v. 17, n. 8, pp. 835-84, 1985

9 J. R. Micol "Langley Aerothermodynamic Facilities Complex: Enhancements and Testing Capabilities," AIAA Paper 98-0147, 36th AIAA Aerospace Sciences Meeting & Exhibit, January 12-15, Reno, NV, 1998.

10 Hollis, B.R. "Real-gas flow properties for NASA Langley Research Center Aerothermodynamics Facilities Complex Wind Tunnels," NASA Contractor Report 4755, Sept. 1996.

11 D.W. Alderfer, P.M. Danehy, J.A. Wilkes Inman, K.T. Berger, G.M. Buck, and R. J. Schwartz, "Fluorescence Visualization of Hypersonic Flow Over Rapid Prototype Wind-Tunnel Models" AIAA Paper 2007-1063, 45th AIAA Aerospace Sciences Meeting and Exhibit, Reno, Nevada, Jan. 8-11, 2007.

12 J. A. Inman, P.M. Danehy, R.J. Nowak, D.W. Alderfer, "Fluorescence Imaging Study of Impinging Underexpanded Jets" AIAA-2008-619, 46th AIAA Aerospace Sciences Meeting and Exhibit, Reno, Nevada, Jan. 7-10, 2008.

13 J. A. Wilkes, D. W. Alderfer, S. B. Jones, and P. M. Danehy, "Portable Fluorescence Imaging System for Hypersonic Flow Facilities," JANNAF Interagency Propulsion Committee Meeting, Colorado Springs, Colorado, December, 2003.

14 R. J. Schwartz, "ViDI: Virtual Diagnostics Interface Volume 1-The Future of Wind Tunnel Testing" Contractor Report NASA/CR-2003-212667, December, 2003.

15 Autodesk 3ds Max Product Information, Autodesk Inc., http://usa.autodesk.com/adsk/servlet/index?id=5659302&siteID=123112, viewed Jan 2, 2006.

16 P. M. Danehy, J. A. Inman, B. Bathel, D. W. Alderfer, S. B. Jones, "Stereoscopic Imaging in Hypersonics Flows using Planar Laser Induced Fluorescence", Paper Number 2008-4267, 26th AIAA Aerodynamic Measurement Technology and Ground Testing Conference, Seattle, WA June 23-26, 2008.

17 S. A. Berry, A. H. Auslender, A. D. Dilley, J. F. Calleja, "Hypersonic Boundary-Layer Trip Development for Hyper-X," J. Spacecraft and Rockets, Vol. 38, No. 6, Nov–Dec, 2001.